6ICEGE 6th International Conference on Earthquake Geotechnical Engineering
1-4 November 2015
Christchurch, New Zealand

Underground Infrastructure Response to Earthquake-Induced Ground Deformation

T.D. O'Rourke[1], J. K. Jung[2], and C. Argyrou[3]

ABSTRACT

The principal causes of earthquake-induced ground deformation are identified and their interaction with underground infrastructure, primarily pipelines and conduits, is described. The coupled forces normal and parallel to underground pipelines arising from earthquake-induced ground movement are evaluated, including a review of measured stresses on pipe surfaces during large-scale testing, evaluation of frictional forces related to soil-pipe interaction, and the resolution of interaction forces along and across pipelines. Methods for characterizing soil reaction to pipe lateral and vertical movements are presented. The maximum downward pipe force is only about one-third the maximum force determined with conventional bearing capacity equations, thus requiring changes in current analytical and design practice. The analytical results for pipeline response to strike-slip and normal fault rupture are shown to compare favorably with the results of both large-scale and centrifuge tests of soil-pipeline interaction simulating these types of severe ground deformation.

Introduction

Earthquake-induced ground deformation is a major concern for underground infrastructure in areas vulnerable to seismic risk. It is also representative of extreme conditions of soil-structure interaction that accompany floods, hurricanes, landslides, large soil movements caused by tunneling and deep excavations, and subsidence resulting from dewatering and/or withdrawal of minerals and fluids during mining and oil production. Hence, pipeline performance during earthquakes provides a framework for the analysis and design of underground infrastructure that is resilient to a variety of natural and construction-related hazards.

This paper focuses on methods for analyzing underground pipeline and conduit response to large permanent ground deformation caused by earthquakes. It begins with a review of the sources of earthquake-induced soil and rock movement and shows how these movements are converted into soil-pipe reactions normal and parallel to the longitudinal axis of the pipeline. Two-dimensional (2D) finite element (FE) analytical approaches are described, and improved methods are presented for 2D modeling of the coupled forces normal and parallel to underground pipelines during large permanent ground displacements. Methods for characterizing soil reaction to pipe lateral and vertical movements are presented with reference to large-scale tests involving pipe lateral and uplift movement in dry and partially saturated sand as well as plane strain FE soil and pipe continuum models. The analytical results for vertical downward movement of pipe in soil are presented. Analytical results for pipeline response to strike-slip and normal fault rupture are

[1]Professor, Sch. of Civil & Envr. Engr., Cornell University, Ithaca, NY, USA tdo1@cornell.edu
[2]Assistant Professor, Civil & Envr. Engr., Youngstown State Univ., Youngstown, OH, USA jai.k.jung@gmail.com
[3]Graduate Research Assistant, Sch. of Civil & Envr. Engr., Cornell University, Ithaca, NY ca353@cornell.edu

shown to compare favorably with the results of both large-scale and centrifuge tests of soil-pipeline interaction simulating these types of severe ground deformation.

Earthquake-Induced Ground Deformation

As described previously (e.g., O'Rourke et al., 2008; O'Rourke, 2010), earthquakes cause transient ground deformation (TGD) and permanent ground deformation (PGD), both of which affect underground infrastructure. TGD is the dynamic response of the ground, and PGD is the irrecoverable movement that persists after shaking has stopped. It may involve pulses of strong motion that locally exceed soil shear and tensile capacity, causing surficial soil cracks and offsets. PGD frequently results in large movements, such as those associated with surface fault rupture, liquefaction-induced lateral spreading, and landslides.

The principal causes and types of TGD and PGD have been summarized by Bird et al. (2004) and are presented in Table 1. In aggregate, they represent the total seismic hazard affecting the performance of underground pipelines and conduits.

To illustrate soil-pipeline interaction, Figure 1a provides a plan view of an underground pipeline deformed by soil mass movement associated with a landslide or liquefaction-induced lateral spread. There is abrupt ground deformation at the margins of the slide/lateral spread where the pipeline is affected by movement oblique to its longitudinal axis. Insert A shows the direction of lateral soil movement, d_H, and horizontal soil reaction force/unit distance, p_H, at the left-hand side of the soil mass. Insert B shows the direction of lateral soil movement and soil reaction force/unit distance, p_H, at the center of the soil mass, where two-dimensional (2D) conditions control the horizontal force mobilized against the pipe. The plane strain conditions of soil-pipe interaction in Insert B are consistent with the large-scale tests and numerical simulations used to estimate the maximum horizontal soil reaction forces and force vs. displacement relationships for lateral soil-pipeline interaction (e.g., Trautmann and O'Rourke, 1985; Jung et al., 2013b). For 2D plane strain soil movement p_H, d_H, and frictional force/unit distance, f_N, are normal to the longitudinal axis of the pipeline.

As illustrated in Insert B, p_H under conditions of oblique soil movement is estimated from the large-scale test results and numerical simulations for 2D plane strain conditions in which lateral force vs. displacement relationships use the component of soil displacement, d_H, normal to the longitudinal axis of the pipeline (parallel to the normal frictional force, f_N). There is ample experimental evidence to justify this approach. Ha et al. (2008) report measured maximum horizontal soil forces under oblique soil movement in centrifuge tests on pipelines subjected to strike-slip fault displacement that compare favorably with those from large-scale 2D plane strain test results. Moreover, bending strains predicted from 2D finite element simulations of pipeline response to strike-slip fault movement compare very well with bending strains measured in large-scale and centrifuge tests of pipeline/strike-slip fault interaction (O'Rourke et al. 2008). The close agreement between experimental and simulated bending strains is noteworthy because bending strains are especially sensitive to p_H.

Table 1: Summary of the principal causes and types of transient and permanent ground deformation associated with earthquakes (Bird et al., 2004)

Type	Cause	Description
Transient	Travelling ground waves	Near surface ground deformation caused by body waves propagating from a seismic source.
	Surface Wave Generation in Large Sedimentary Basins	Surface waves generated by scattering incoming waves in large sedimentary basins typically several km wide, with depths < 1 km.
	Vibration of relatively narrow soil-filled valleys	Deformation of sediment-filled valleys with respect to relatively rigid valley boundaries. Valley width and depths are typically several hundred and several tens of meters, respectively.
	Ridge shattering	Ground disturbance along steep ridges and elevated topography that may be accompanied locally by slip in fractured rock.
	Ground oscillation	Transient lateral shear strains and horizontal movement of liquefiable soil relative to adjacent and underlying competent material.
Permanent	Faulting	The principal components of fault movement include 1) strike, 2) reverse, and 3) normal slip. Reverse and normal faults promote compression and tension, depending on the angle of intersection between lifelines and the fault trace.
	Tectonic Uplift and Subsidence	Regional changes in dimension associated with crustal deformation. Deformation occurs over a long distance so strains imposed will be small. Subsidence adjacent to water bodies can flood sections of a lifeline and possibly lead to erosion and undermining.
	Liquefaction	Displacement caused by transformation of saturated, cohesionless soils to liquefied state or condition of substantially reduced shear strength. Liquefaction-induced lifeline deformation can be caused by 1) lateral spread, 2) flow failure, 3) local subsidence, 4) post-liquefaction consolidation, 5) buoyancy effects, and 6) loss of bearing.
	Landslides	Mass movement of the ground triggered by inertial forces from seismic shaking. Many displacement patterns are possible. Principal forms of movement include 1) rock falls, 2) relatively shallow slumping and sliding of soil, and 3) relatively deep translation and rotation of soil and rock. Landslides include lurching and soil block movement in which ground displacements are triggered by transient loading of gently sloping deposits underlain by weak soil not susceptible to liquefaction.
	Densification	Decrease in volume caused by seismic vibration of dry or partially saturated cohesionless soil.

The frictional force, f_T, generated in granular soil during oblique soil movement is decomposed into its parallel component as $f_P = f_T\cos\beta$ to obtain the frictional force along the longitudinal axis of the pipeline. The frictional force component normal to the pipeline longitudinal axis is $f_N = f_T\sin\beta$, which represents the friction dissipated as soil displaces around the pipe. Thus, the parallel and normal components of f_T, depend on the angle, β, which defines the obliquity of soil movement relative to the pipeline. Please note that f_T is a vector, which is aligned in the same orientation as the oblique soil displacement, d_T.

The three-dimensional (3D) view in Figure 1b shows a different orientation in which the pipeline is subjected to axial compression and tension at opposite sides of the moving soil mass. A pipeline crossing the margin of a slide/lateral spread is similar to one crossing an active strike-slip fault. The vector frictional force, f_T, is decomposed into normal and parallel components in the same way for both conditions of earthquake-induced soil deformation.

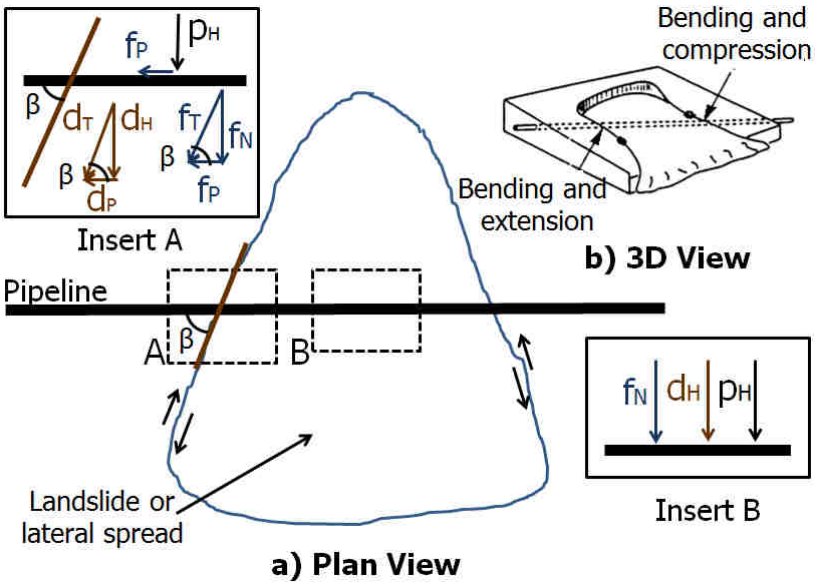

Figure 1. Plan and 3D views of pipeline intersection with landslide or lateral spread

Pipeline Frictional Forces

For a pipeline at rest in cohesionless soil, it is well established (e.g., ASCE, 1984) that the maximum frictional force per unit distance along the pipeline longitudinal axis, f_{pmax}, is given by

$$f_{p\max} = 0.5(1+K_0)\overline{\gamma}H_c\pi D\tan\delta \qquad (1)$$

in which H_c is the depth to pipe centerline, $\overline{\gamma}$ is the soil unit weight contributing to effective stress at the pipe centerline, K_0 is the coefficient of at-rest horizontal soil stress (generally $0.5 \leq K_0 \leq 1.0$ for pipe in backfilled trenches), δ is the angle of interface frictional resistance, and D is the pipe outside diameter. This force, f_{pmax}, is mobilized to resist axial pipeline deformation where at-rest conditions exist outside the area of major soil deformation, such as the landslide/lateral spread illustrated in Figure 1.

When a pipeline or conduit is intersected by soil movement, the at-rest conditions are disrupted, and the pipeline is subjected to frictional force directly related to the distribution of stresses normal to the pipe surface and indirectly related to p_H, which is the soil reaction force normal to the pipeline longitudinal axis.

To understand how p_H is related to the fictional force on the pipeline, pipe surface stress measurements with tactile pressure sensors are examined. As described by Palmer et al (2009), a tactile pressure sensor is an array of small sensing units, called sensels, embedded in a polymeric sheet or pad that measures the magnitude and distribution of stresses normal to the sheet surface. Measurements with these sensors during large-scale 2D tests of soil-pipe interaction under relative horizontal displacement, δ_H, between pipe and soil (Palmer et al., 2009) were analyzed in accordance with Figure 2.

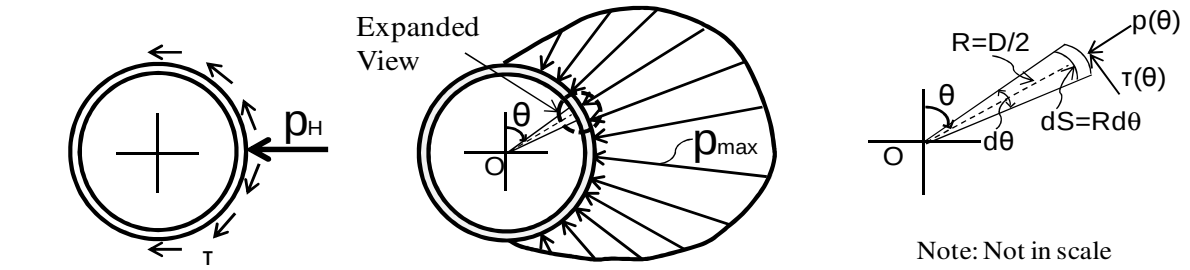

a) Shear Stress Orientation b) Normal Stress Distribution c) Expanded View

Figure 2. Lateral soil- pipe interaction model for underground pipelines (Palmer et al., 2009)

If $p(\theta)$ denotes the soil stress normal to the pipe surface as a function of angular position around the circumference, θ, and $\tau(\theta)=p(\theta)\tan\delta$ is the frictional shear stress, p_H is obtained by integrating the horizontal components of $p(\theta)$ and $p(\theta)\tan\delta$ as follows

$$p_H = \frac{D}{2}\left[\int_0^{2\pi} p(\theta)\sin\theta d\theta + \tan\delta\int_0^{2\pi} p(\theta)\cos\theta d\theta\right] \quad (2)$$

The net horizontal force per unit length, p_H, can also be obtained from the experimental data using the following relation

$$p_H = \sum_{j=1}^{J}(p_m)_j S_j \sin\theta_j + \tan\delta\sum_{j=1}^{J}(p_m)_j S_j \cos\theta_j \quad (3)$$

in which $(p_m)_j$ is the measured pressure, p_m, at the j-th pressure sensor node, S_j is the arc length associated with the j-th pressure sensor node ($S_j = 2\pi R/J$), $(p_m)_j$ is the angle defining the orientation of $(p_m)_j$, and J is the total number of pressure sensor nodes around the pipe surface per unit length.

Normal stress measurements taken by Palmer et al. (2009) for soil-pipe interaction in dry sand were normalized with respect to the maximum normal stress, p_{max}, and regressed with the sinusoidal curve fitting techniques described in Appendix A to obtain distributions of measured normalized stress, $p(\theta)/\ p_{max}$. Two sets of measurements were regressed from tactile pressure sensors, denoted as Sensors B and Sensor A, located at the midpoint and a distance of ¼ the test pipeline length from its midpoint, respectively. The two datasets showed slightly different normalized pressure distributions, and were selected to cover variations in pressure measured along the test pipeline.

Figures 3a is a plot of the transformed normalized pressures measured by Sensor A regressed with respect to angular distance, θ, from the pipe crown, as defined in the insert diagram. The linear regression involves rising and falling portions that are fit to the data by the least squares method. The slope, ω_o, and intercept, Δ, are labeled. The regression analyses were originally performed on 24 and 12 different measurements at different levels of lateral soil movement for Sensor A and B, respectively. Data points falling outside two standard deviations from the mean

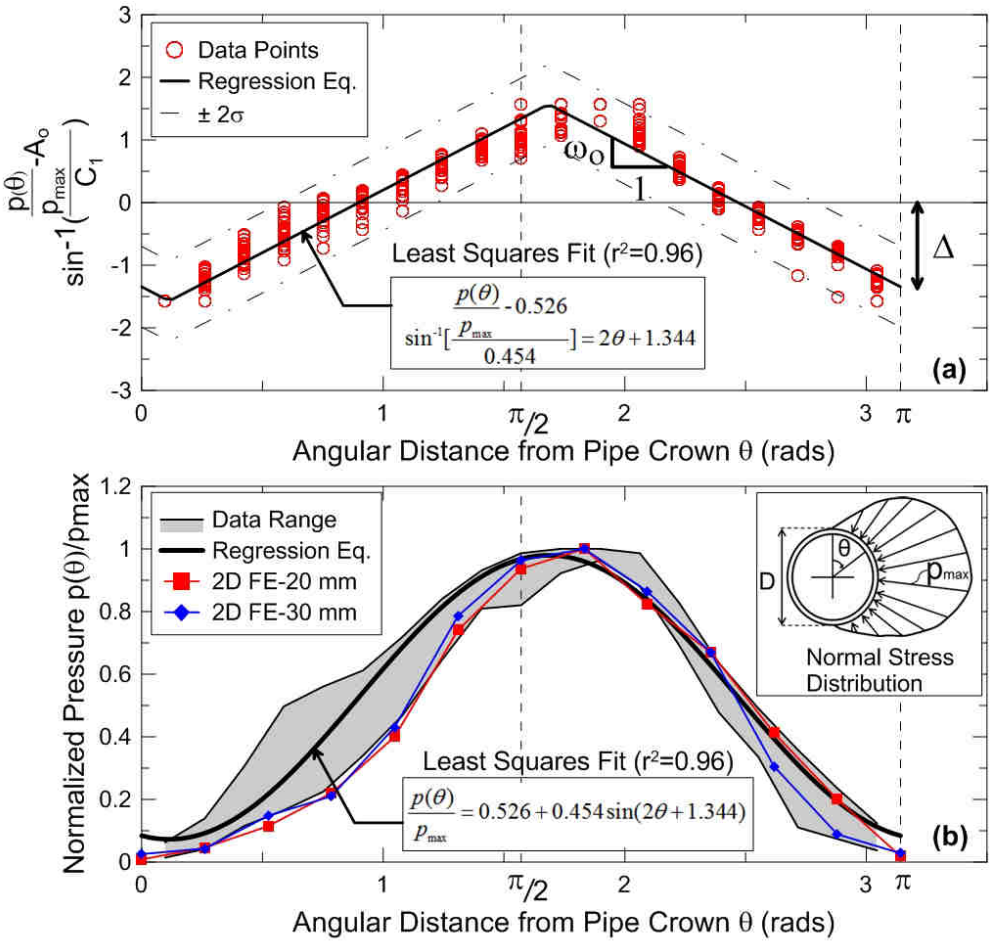

Figure 3. Normalized pressure vs. angular distance for (a) linear regression with transformed normalized pressure and (b) sinusoidal pressure distribution

were screened to remove unrepresentative measurements. In each case, two to three erratic measurements were screened from the data at relatively low levels of lateral pipe movement before the maximum horizontal force was established.

The regression equation obtained from Figure 3a is plotted in Figure 3b with respect to the range of measured values. Also plotted in the figure are the normalized pressure distributions from finite element (FE) simulations using pipe shell and soil continuum elements performed by Jung et al. (2013b) for the same large-scale 2D test reported by Palmer et al. (2009). The FE results correspond to 20 and 30 mm of relative horizontal pipe displacement, which is consistent with the relative displacements pertaining to the experimental data. The analytical and experimental normalized pressures are in close agreement.

For Sensor A, the normalized pressure distribution (r^2=0.96) is given by

$$\frac{p(\theta)}{p_{max}} = 0.526 + 0.454\sin(2\theta + 1.344) \quad (4)$$

The total normal force per unit distance, p_N, acting on the pipe can be calculated as the product of the maximum pressure and integration of the normalized stress distribution. Similarly, p_H, can be determined by means of Eqs. 2 and 3. Both numerical integration of tactile pressure sensor measurements and closed form integration of Eq. 4 are in excellent agreement, yielding

$$p_N = \frac{D}{2} p_{\max} \int_0^{\pi} \frac{p(\theta)}{p_{\max}} d\theta = 1.636 \frac{D}{2} p_{\max} \tag{5}$$

$$p_H = \frac{D}{2} p_{\max} \left[\int_0^{\pi} \frac{p(\theta)}{p_{\max}} \sin\theta d\theta + \int_0^{\pi} \frac{p(\theta)}{p_{\max}} \tan\delta \cos\theta d\theta \right] = \frac{D}{2} p_{\max} (1.346 + 0.741 \tan\delta) \tag{6}$$

The total frictional force, f_T, is the product of the normal force acting on the pipe and tan δ of the pipe surface, as follows

$$f_T = p_N \tan\delta = 1.636 \frac{D}{2} p_{\max} \tan\delta \tag{7}$$

The apparent frictional force per unit pipe length, f_A, can be defined as

$$f_A = \mathrm{p}_H \tan\delta = \frac{D}{2} p_{\max} (1.346 + 0.741 \tan\delta) \tan\delta \tag{8}$$

It is convenient to estimate the longitudinal friction force during numerical simulation as the product of the force normal to the longitudinal pipeline axis and tanδ. Therefore, the ratio, f_T / f_A, is a correction factor that can be applied to the apparent friction, f_A, to reflect the total friction acting on the pipe. Combining Eqs. 7 and 8 results in

$$\frac{f_T}{f_A} = \frac{1.636}{1.346 + 0.741 \tan\delta} \tag{9}$$

Figure 4 shows f_T / f_A relative to tan δ for both Sensor A and B measurements. For polyethylene and polyvinyl chloride pipelines as well as pipelines with polyethylene or fusion epoxy coatings, tanδ ranges between 0.4 and 0.6. As shown in Figure 4, f_A and f_T are in close agreement for this range of tanδ. For concrete pipelines, pipelines with mortar coatings, and metallic pipelines without coatings tanδ typically is between 0.7 and 1.0 so that f_A is a conservative overestimate of f_T by about 15 – 22%.

Figure 4 indicates that p_H tanδ can be used to estimate the longitudinal frictional force on a pipeline with little to no error when $0.4 \leq \tan\delta \leq 0.6$ and to provide a conservative estimate when tanδ > 0.7. A reliable estimate of longitudinal frictional force, therefore, requires a coupled analysis in which p_H and tanδ are combined. It is often assumed that the at-rest conditions given by Eq. 1 apply along the entire pipeline for 2D pipeline response to soil movement. This assumption is not accurate in areas of major soil deformation, such as the landslide/lateral spread shown in Figure 1, and will result in an unconservative estimate of maximum axial pipe strain.

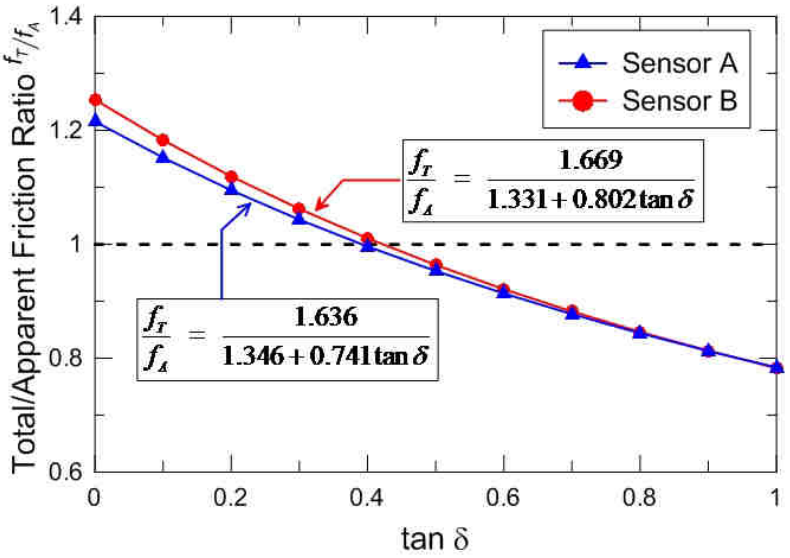

Figure 4. Ratio of total to apparent friction f_T/f_A vs. $\tan\delta$

Lateral and Uplift Soil-Pipe Interaction

A comprehensive program of large-scale tests and FE modeling was undertaken to evaluate the maximum soil reaction force and force vs. displacement relationships for lateral and uplift movement of pipelines in dry and partially saturated sand (O'Rourke et al., 2008; O'Rourke, 2010). Reference should be made to Jung et al. (2013a and 2013b) for a detailed presentation of experimental and analytical findings. Only the salient features of the large-scale testing, FE modeling, and program results are provided in this paper.

Numerous large-scale tests were performed at the Large-Scale Lifelines Testing Laboratory at Cornell University, which was originally part of the George E. Brown Network for Earthquake Engineering Simulation (O'Rourke et al., 2008). The tests were performed in conjunction with tests using the 150 g-ton centrifuge at Rensselaer Polytechnic Institute (RPI). The test results were used to develop relationships between maximum soil reaction forces, sand density, and pipe depth/diameter as well as to validate FE models for lateral and uplift pipe movement in sand.

Soil-pipeline interaction for lateral and uplift pipe displacement in granular soil was evaluated by means of a two-dimensional, finite element (FE) continuum model with a Mohr-Coulomb (MC) yield surface for peak strength, a strain softening relationship tied to critical void ratio, and an equivalent modulus that is consistent with soil deformation at maximum lateral and uplift resistance. A systematic comparison of FE model results with multiple full-scale test measurements show excellent agreement both with respect to maximum force and force-displacement relationships, including post-peak performance (Jung et al., 2013a and 2013b).

Table 2. Summary of representative peak angles of shear resistance and angles of dilatency for medium, dense, and very dense sand

Density	γ_δ[1] (kN/m^3)	ψ_p[2] (degrees)	$\phi'_{ds\text{-}p}$[3] (degrees)	$\phi'_{ps\text{-}p}$[4] (degrees)
Medium	16	3 ~ 6	35 ~ 37	41 ~ 44
Dense	17	7 ~ 10	38 ~ 40	45 ~ 47
Very Dense	18	11 ~ 17	41 ~ 43	48 ~ 49

1 – γ_d = dry soil unit weight
2 – ψ_p = peak angle of dilatency
3 – $\phi'_{ds\text{-}p}$ = direct shear peak angle of shear strength
4 – $\phi'_{ps\text{-}p}$ = plane strain peak angle of shear strength

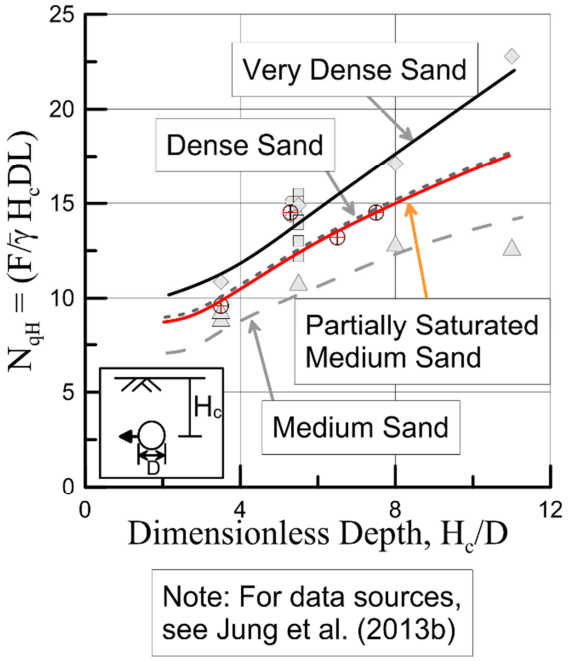

Figure 5. Maximum dimensionless lateral pipe force

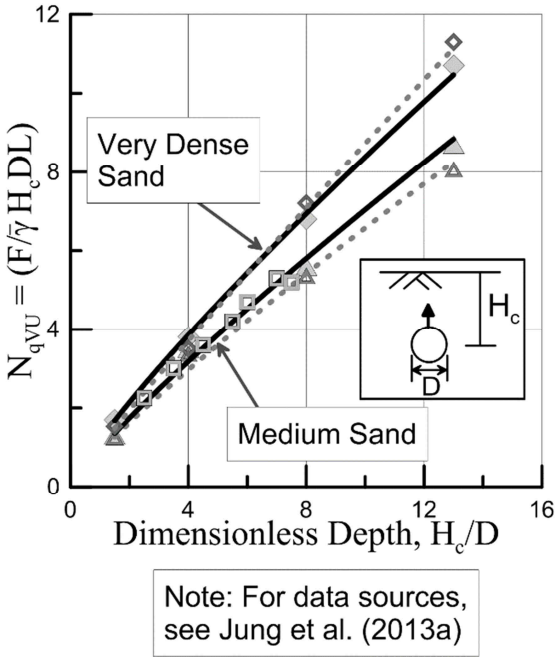

Figure 6. Maximum dimensionless uplift pipe force

Figure 5 presents plots of the maximum dimensionless lateral pipe force, N_{qH}, vs dimensionless depth, H_c/D, for dry medium, dense, and very dense sand for $H_c/D \leq 11$, based on the large-scale test and analytical results provided by Jung, et al. (2013b). Soil properties for medium, dense, and very dense sand are summarized in Table 2. The dimensionless maximum pipe force is expressed as $F/(H_c\,\bar{\gamma}DL)$ for which F = soil-pipe reaction force, $\bar{\gamma}$ = soil unit weight contributing to effective stress at the pipe centerline, H_c = depth to pipe center, D = outside pipe diameter, L = pipe length. Figure 5 also contains a plot of N_{qH} vs H_c/D for partially saturated medium dense sand as reported by Jung et al. (2013b). Pipelines are most often constructed in unsaturated soils, where a meniscus forms between soil particles, creating suction that binds the particles together. A direct comparison of N_{qH} for dry and partially saturated medium sand provides an estimate of the increased lateral force related to suction for the grain size characteristics of the test sand.

Figure 6 presents plots of the peak dimensionless uplift pipe force, N_{qUV}, vs. dimensionless depth, H_c/D, for dry medium and very dense sand for $H_c/D \leq 13$, based on the large-scale test and analytical results provided by Jung, et al. (2013a). The analytical model developed by Jung et al. (2013a) accounts for soil migration beneath the pipe through FE mesh adjustment coordinated with upward pipe displacement. For $H_c/D \leq 5.5$, the model predicts decreasing uplift force after a peak value as upward movement of the pipe continues, which is consistent with experimental measurements. Similar to the comparison of analytical and experimental results for lateral soil-pipe interaction, a systematic comparison of FE model results with multiple full-scale test measurements of pipe response to uplift displacement in dry sand show excellent agreement both with respect to maximum force and force-displacement relationships.

Vertical Soil-Pipe Interaction

Because large-scale 2D experimental results are not available for downward pipe movement in soil, FE analyses were used to simulate this mode of soil-pipe interaction. The FE modeling approach, which is described in detail by Jung (2010), was validated by simulating the vertical load response of deep foundation bearing elements and confirming that they compare favorably with the tip resistances of similar deep foundations as calculated from widely used bearing capacity formulations (e.g., Kulhawy et al., 1983).

Approximately 1500 to 5000 elements were used in each FE simulation, depending on H_c/D conditions. Infinite elements (Zienkiewicz et al., 1983), were used to represent a semi-infinite soil medium, and the pipe was modeled as a rigid cylinder, with a soil/pipe interface friction angle of $0.6\phi'_{ds\text{-}p}$, as reported by several researchers (e.g., Trautmann and O'Rourke, 1985, Trautmann et al., 1985). Pipe movement was generated by imposing vertical downward displacements on all pipe nodes. Separation and slip between soil and pipe were allowed in the analysis, and geostatic loading under K_o=1 conditions was applied to the soil and pipe at the beginning of each FE simulation. Methods recommended for the interpretation of deep and shallow foundation load tests (Akbas and Kulhawy, 2009a) were used to identify the maximum vertical force from the load vs settlement results for each simulation.

Figure 7 presents the FE results for the dimensionless maximum vertical downward force (N_{qVD}) related to medium, dense, and very dense sand for H_c/D = 2–11. As H_c/D decreases, N_{qVD} approaches a value analogous to the bearing capacity of a circular dished foundation with width D at the ground surface.

Guidelines for the seismic design of oil and gas pipelines recommend that the maximum vertical force associated with downward pipe movement be estimated by conventional bearing capacity formulations (ASCE, 1984; Honegger and Nyman, 2004). It is of interest therefore to compare the maximum vertical pipe force from conventional bearing capacity theory with the peak pipe force given by the FE simulations.

The pipe bearing capacity was calculated according to widely used bearing capacity formulations (e.g., Kulhawy et al., 1983 and Akbas and Kulhawy, 2009b), which show that the maximum tip resistance of a deep foundation, $Q_{tc\text{-}bc}$, can be estimated as

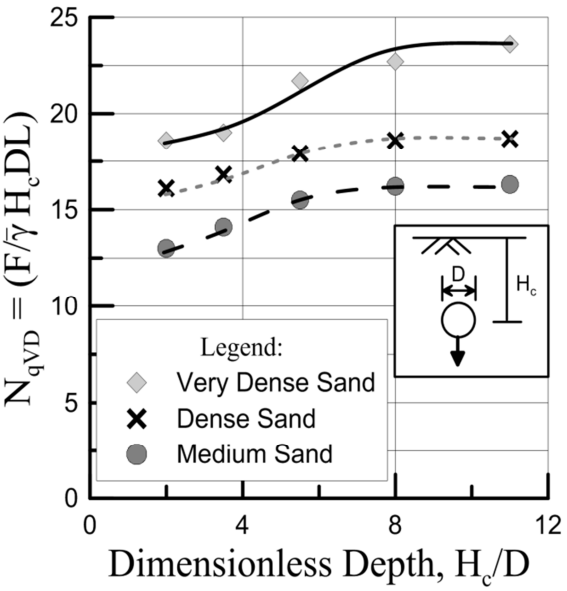

Figure 7. Finite element dimensionless maximum vertical downward force

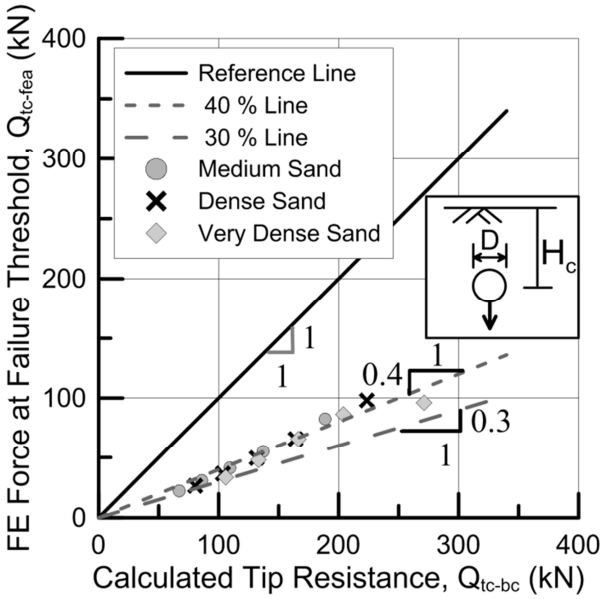

Figure 8. Finite element vertical force vs. bearing capacity vertical force

$$Q_{tc-bc} = \left(qN_q\xi_{qr}\xi_{qs}\xi_{qd}\xi_{qi}\xi_{qg}\xi_{qt}\right)A_{tip} \quad (10)$$

in which q = vertical effective stress at H_c, N_q = bearing capacity factor, ξ_{qr} = rigidity factor, ξ_{qs} = shape factor, ξ_{qd} = depth factor, ξ_{qi} = load inclination factor, ξ_{qg} = ground surface inclination factor, ξ_{qt} = tilt of foundation factor, and A_{tip} = area of the base of the foundation. For this study, the ξ_{qi}, ξ_{qg}, ξ_{qt} factors were equal to 1.0 because all analyses were conducted for level ground without any load inclination or eccentricity.

The bearing capacity vertical forces, Q_{tc-bc}, were calculated with Eq. 10 for medium, dense, and very dense sand at H_c/D = 8, 11, 15, 20, and 30. The peak force from each FE analysis, Q_{tc-fea}, is plotted with respect to Q_{tc-bc} for H_c/D = 8–30 in Figure 8. As shown in the figure, the failure threshold force for 2D pipe settlement is consistently lower than the bearing capacity force for a deep foundation, with Q_{tc-fea} approximately 1/3 of Q_{tc-bc}.

The bearing capacity vertical forces, Q_{tc-bc}, were calculated with Eq.10 for medium, dense, and very dense sand at H_c/D = 8, 11, 15, 20, and 30. The peak force from each FE analysis, Q_{tc-fea}, is plotted with respect to Q_{tc-bc} for H_c/D = 8–30 in Figure 8. As shown in the figure, the failure.The value of Q_{tc-fea} is relatively low because downward pipe movement is accompanied by soil migration into a zone in the soil mass directly above the pipe. Such movement is markedly different from what occurs during deep foundation settlement, when soil migration cannot occur into a zone immediately above the base of the foundation. As a result, there are substantially higher constraints on soil deformation with higher resistance to tip penetration of the soil mass.

Simulation of Coupled Normal and Frictional Forces

As explained previously, at-rest conditions are disrupted when a pipeline or conduit is intersected by soil movement. In response to large ground deformation, an underground pipeline is subjected to frictional force directly related to the soil reaction force normal to the pipeline longitudinal axis. Figure 4 shows that the apparent frictional force, $f_A = p_H \tan\delta$, will provide a close estimate of the actual frictional force, f_T, when $\tan\delta$ is between 0.4 and 0.6, and will provide a conservative estimate when $\tan\delta > 0.6$. To account for elevated frictional resistance as p_H increases, the FE simulation must couple the normal and frictional forces. The need for coupling normal and frictional forces applies for lateral, upward, and downward pipe displacement.

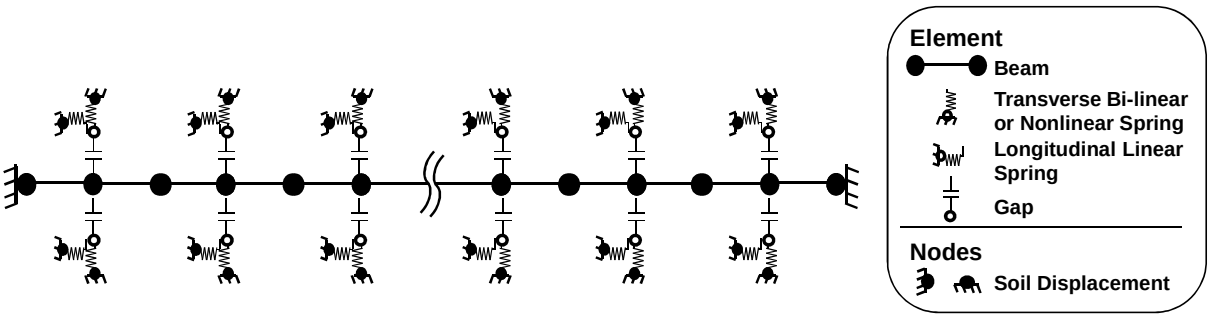

Figure 9. 2D FE model setup for coupled forces normal and parallel to a pipeline under PGD

Figure 9 shows a schematic of the proposed 2D FE model, which was developed in this work with the software ABAQUS (2014) to account for coupled normal and frictional forces. The pipeline is represented by beam elements (type b33) and the soil resistance normal to the pipeline axis by nonlinear springs (type spring2). The springs are connected to the pipeline with uniaxial gap elements (type gapuni), which are interface elements allowing for the transfer of forces parallel and perpendicular to their axes. The gap elements are aligned in a direction perpendicular to the pipeline axis, as shown in Figure 9, and were modeled to transfer forces only when the corresponding normal springs carry compressive forces. This is achieved by allowing separation of the gap elements when tensile normal forces are activated in response to load relaxation and separation between soil and pipe. This modeling is important for the simulation of pipeline response to normal faulting where considerably different soil reaction forces are mobilized on the upthrown and downthrown sides of the fault. It is also important for simulating the effects of severe differential settlement.

The normal force per unit distance, p_N, transferred through the gap element parallel to the pipeline longitudinal axis is controlled by a simple Coulomb friction law, $p_N \tan\delta$, forcing it to be proportional to the normal force acting on the pipeline at each level of deformation. Transverse nonlinear or bi-linear springs account for force vs. displacement relationships for lateral, uplift, and downward pipe movement. The longitudinal springs follow a linear force vs. displacement relationship with a high spring constant and are required only to transfer the input soil displacement. The soil resistance parallel to the pipe is controlled by the gap element, as described above.

In the FE model, as an initial step, the displacements required to activate the normal forces for at-rest conditions are imposed on the transverse springs. With this adjustment, longitudinal frictional forces are activated when there is relative soil displacement along the pipeline, even in the absence of normal forces triggered by relative normal soil displacement. During the simulation, incremental parallel and normal soil movements are applied simultaneously at the longitudinal and transverse spring nodes on each side of the pipeline elements.

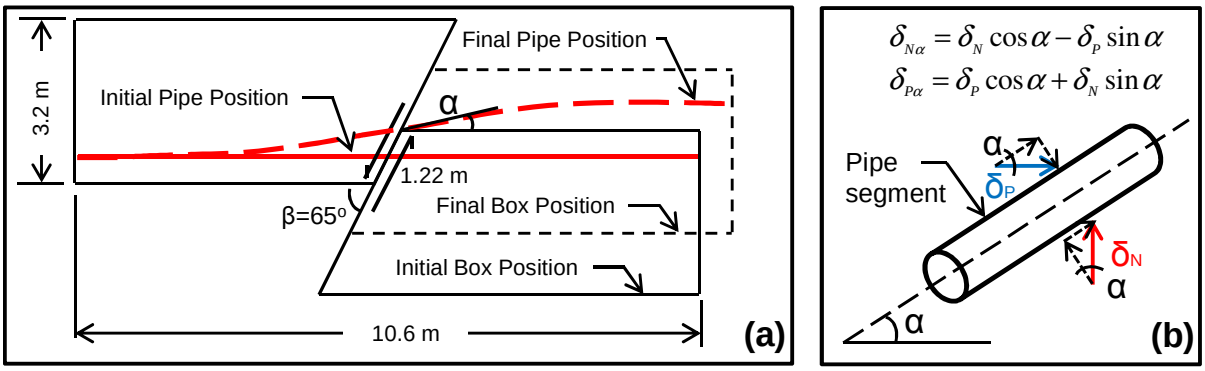

Figure 10. Plan view of large-scale pipeline test showing (a) key dimensions and geometry, and (b) relative pipeline displacements

Simulation of Pipeline Response to Strike-Slip Fault Movement

Large-scale tests are described by O'Rourke et al. (2008) in which high density polyethylene (HDPE) pipelines were subjected to 1.22 m of strike-slip displacement at a vertical fault crossing angle of 65°, as illustrated in Figure 10a. The tests were performed on nominal 250-mm and 400-mm diameter pipelines at a 1-m depth to pipe centerline. The outside diameter was 272 mm and 407 mm for the 250-mm and 400-mm pipe, respectively. The wall thickness was 24.9 mm for both. The 13.2-m-long, 3.2-m-wide and 2.3-m-high split-basin test facility can generate maximum fault displacements of 1.2 to 1.8 m. All split-basin tests were conducted with partially saturated sand with dry unit weight and moisture content of 15.7 kN/m^3 and 4%, respectively. Each pipeline specimen was instrumented with over 100 strain gages.

Pipeline response to strike-slip faulting was simulated with an FE model composed of 43 beam elements (type b33), 168 spring elements (type spring2), and 84 gap elements (type gapuni). Strain rate and temperature effects of the HDPE were taken into account with stress vs. strain data from direct tension tests in an environmental chamber under constant temperature and strain rates. The stress vs strain results for a strain rate of 10%/min. at 21ºC was found to match best the actual strain rate (2%/min) and temperature (26º C) associated with the full-scale tests. The analyses were performed with maximum soil forces for dry medium dense sand in Figure 6 and bilinear force vs. displacement relationships as described by Jung et al. (2013a, 2013b).

As illustrated in Figure10a, the orientation of the pipeline near the fault changes with respect to the direction of soil movement as the strike-slip offset increases. Figure 10b shows how the initial relative normal and parallel soil displacements, δ_N and δ_P, respectively, change as the orientation α, of a pipeline segment alters from its initial orientation at $\alpha = 0$. The figure shows

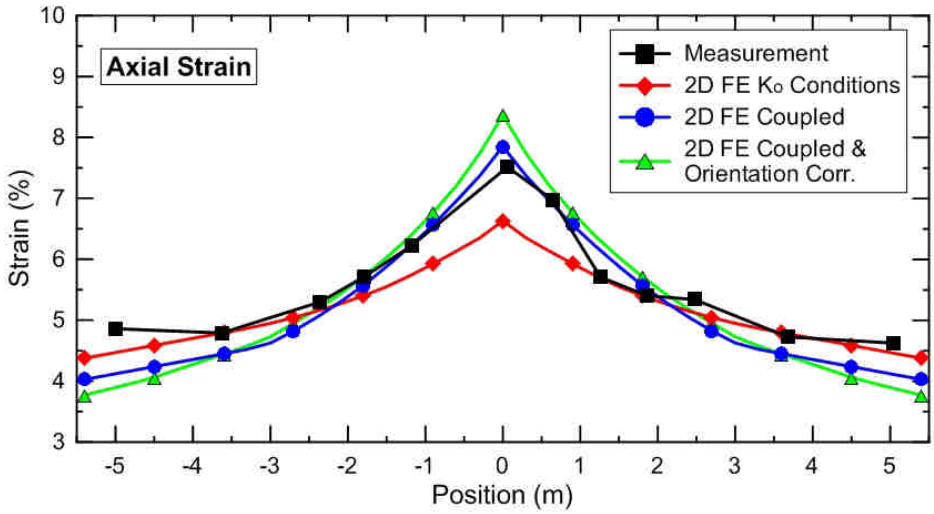

Figure 11. Measured and numerical axial strains in a 250-mm HDPE pipe under strike-slip faulting for various FE models

how the initial relative displacements, δ_N and δ_P, are decomposed into directions normal and parallel to the pipe to provide the relative normal and parallel displacement $\delta_{N\alpha}$ and δ_{Pa}, respectively, at any pipe segment orientation, α. If $\tan\psi_\alpha = \delta_{N\alpha}/\delta_{P\alpha}$, then

$$\tan\psi_\alpha = \frac{\delta_N \cos\alpha - \delta_P \sin\alpha}{\delta_N \sin\alpha + \delta_P \cos\alpha} \tag{11}$$

which is simplified as

$$\tan\psi_\alpha = \frac{\tan\psi - \tan\alpha}{\tan\psi \tan\alpha + 1} \tag{12}$$

from which

$$\psi_\alpha = \tan^{-1}\left(\frac{\tan\psi - \tan\alpha}{\tan\psi \tan\alpha + 1}\right) \tag{13}$$

Please note that $\tan\psi = \delta_N/\delta_P$, the ratio of normal and parallel relative displacements at the beginning of fault movement when $\tan\psi = \tan\beta$ and β is the pipeline/fault angle of intersection. Treating friction as a unit vector, $\cos\psi_\alpha$ is the fraction of the total frictional force, f_T, along the pipeline longitudinal axis.

To account for the effects of pipe rotation, ψ_α was calculated at each pipeline node, for which cos ψ_α was calculated at various levels of strike-slip movement. The average value for cos ψ_α was then used at each FE pipe node to estimate the frictional force along the pipeline longitudinal axis. As fault displacement increased, the angle between the fault and pipe segment near the fault decreased, thereby increasing cos ψ_α and the magnitude of friction mobilized along the pipe. Outside the zone of changing α, at-rest conditions were assumed in accordance with Eq. 1.

Figure 11 compares the measured axial strains with FE results for 1) at-rest conditions with no coupling between normal and frictional forces (denoted as "K_0 Conditions" in the figure), 2) coupled normal and frictional forces (denoted as "Coupled"), and 3) coupled normal and frictional forces with corrections for pipe orientation, α (denoted as "Coupled & Orientation Corr."). The apparent frictional force, $f_A = p_H \tan\delta$, was used to estimate frictional force in the absence of orientation corrections, with $\tan\delta = 0.44$ in accordance with HDPE/sand direct shear measurements reported by Olson (2009).

Axial strains from FE simulations with coupled normal and frictional pipe forces are in close agreement with the measurements. There is less than 5% difference between maximum FE and measured axial strain. Axial strains from FE simulations with coupled forces and pipe orientation corrections are also in close agreement with measured strains, but overestimate maximum axial strain. Correction for pipe orientation has a relatively small effect on the analytical outcome. The axial strains analyzed with at-rest (K_0) conditions of longitudinal friction (see Eq. 1) and no coupling of forces underestimates the measured axial strain by approximately 12%. The differing approaches to modeling longitudinal friction have little effect on bending strains, which are highly dependent on p_H modeling that was the same for all FE results. In general, the differences among the analytical and measured bending strains are less than 5%.

Analytical and Experimental Results for Strike-Slip Fault and Normal Fault Movements

Simulations of soil-pipeline interaction under strike-slip and normal fault displacements were performed using coupled normal and frictional forces. Corrections for pipe orientation near strike-slip faulting were not used because these adjustments have a relatively minor effect on the analytical results, as discussed above. The numerical results are presented for lateral force vs. displacement relationships presented by Jung (2010) and Jung et al. (2013b) with maximum lateral loads for both dry and partially saturated medium dense sand taken from Figure 6. The numerical results are compared with pipeline strain measurements reported by O'Rourke at al. (2008) from large-scale strike-slip soil movements on HDPE pipelines conducted in the split-basin test facility at Cornell University. The numerical results for normal faulting are compared with the results of a centrifuge test at RPI described by Ha (2007) and Xie at al. (2013). The experimental conditions, including soil properties, pipeline characteristics, and split-basin dimensions, are described in the previous section of this paper. Likewise, the characteristics of the finite element model are described in the previous section.

Figures 12a and b compare the numerical and measured axial and bending strains for large-scale tests on a 250-mm and two 400-mm HDPE pipelines, respectively, at 1.22 m of strike-slip displacement. Axial strains are calculated as the average pipe crown and invert strains, and bending strains are determined as one half the difference between the springline strains. Insert diagrams in the figure show the crown, springline, and invert locations.

There was a short distance along the pipeline (~ 1m) where a tactile pressure sensor was installed and strain gages were absent, as shown in Figure 12a. The numerical and experimental bending strains follow similar distributions and are virtually identical in magnitude. The numerical and experimental axial strains likewise follow similar distributions, with the maximum FE axial strain for dry and partially saturated conditions between 5 and 10 % higher, respectively, than the measured axial strain.

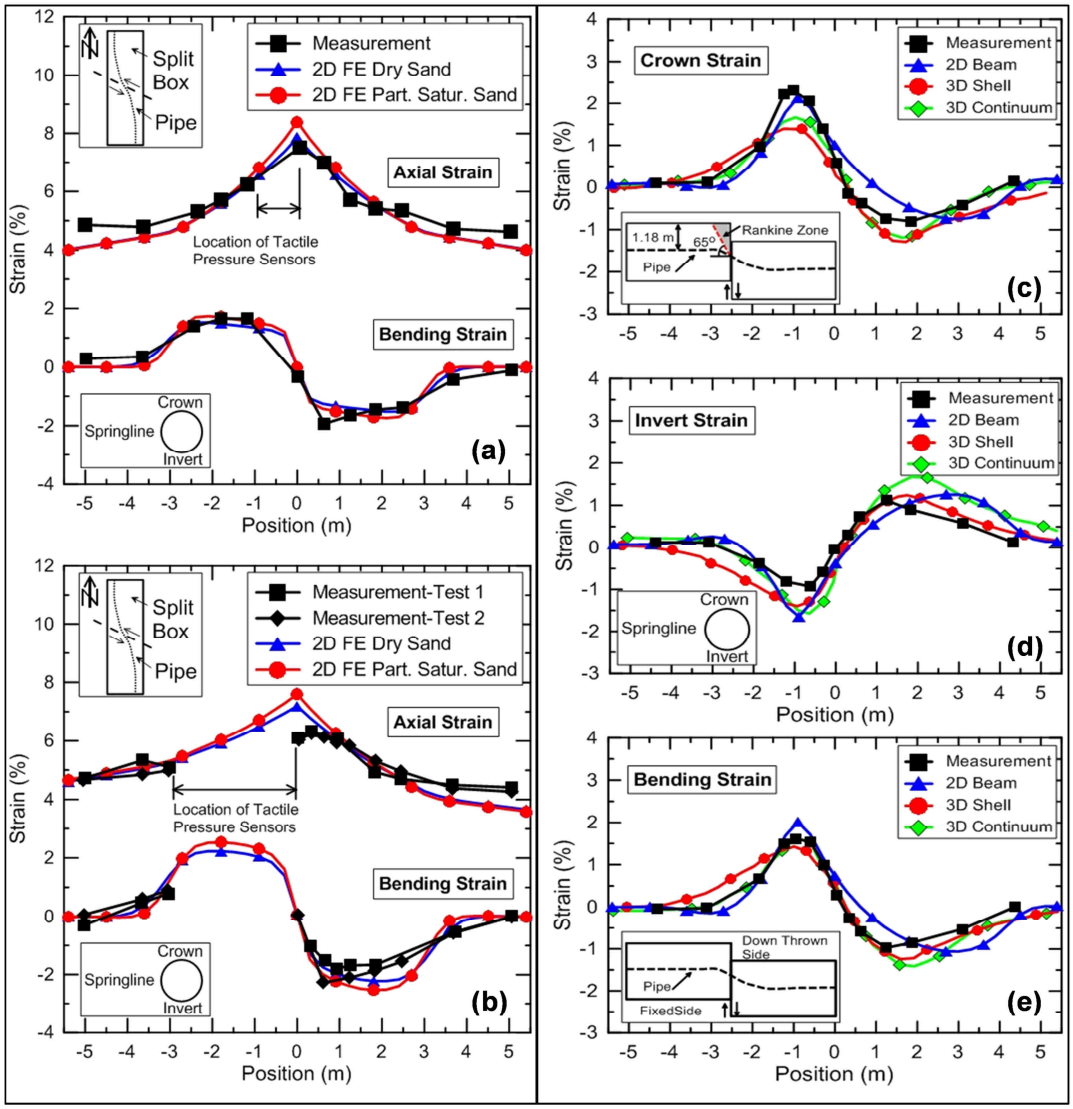

Figure 12. Measured and numerical simulated strains for large-scale testing of (a) 250-mm and (b) 400-mm HDPE pipelines and (c)-(e) centrifuge test of 400-mm HDPE pipeline

Figure 12b presents the measured and simulated strains for two 400-mm-diameter HDPE pipelines. Several tactile pressure sensors were installed south of the fault rupture, as shown in the figure. A double layer of Teflon sheets was used to protect the sensors, and resulted in a sizeable zone where very low shear stress was transmitted to the sensor and pipe. Reduced longitudinal friction in this zone was modeled by tan δ = 0.1- 0.2 to represent the effect of the Teflon sheets. With nearly half the pipeline south of the ground rupture isolated from the full effects of soil shear forces, additional load was conveyed asymmetrically to each end of the test pipelines, with higher axial strains at the south end. This asymmetric distribution of axial strain is well represented by the FE results. Measured strains at the center of the pipeline appear to be influenced by the adjacent tactile pressure sensor, but otherwise are mostly within 10% of the analytical values.

Figures 12c, d, and e compare FE and centrifuge measured strains for a prototype 400-mm-nominal-diameter HDPE pipeline subject to normal fault displacement. Numerical simulation of the centrifuge test with 2D and 3D FE soil-pipeline interaction models is described in detail by Xie et al. (2013). Centrifuge testing was performed at 12.2 g with a split-box container fabricated for in-flight simulation of fault rupture (Ha, 2007). A maximum prototype displacement of 0.48 m was imposed as abrupt vertical movement of one side of the container relative to the other (see insert diagram in Figure 12e). The prototype depth to pipe centerline was approximately 1.2 m in partially saturated sand with dry unit weight and moisture content of 14.7 kN/m^3 and 4%, respectively. The centrifuge tests were conducted with the same HDPE properties, diameter, and thickness as the pipe in the large-scale Cornell experiments described above.

The 2D FE model used in this work to simulate the experiment was composed of 47 beam elements (type b33), 184 spring elements (type spring2) and 96 gap elements (type gapuni) that account for coupled normal and frictional forces. The stress vs. strain relationship for the HDPE behavior corresponding to 1% loading rate at 21° C, as reported by Ha (2007) was used in the simulations. The analysis was performed with uplift and vertical downward forces from Figures 6 and 7 for medium sand and bilinear force vs. displacement relationships (Jung, 2010; Jung at al., 2013a). Because the burial depth was relatively shallow with $H_c/D = 2.7$, uplift forces decreasing after a peak force were modeled in accordance Jung et al. (2013a). The vertical displacement was distributed linearly from the edge of the Rankine active zone on the upthrown side of the fault (see insert diagram in Figure 12c) to the maximum downward movement at the fault plane. For the reported 40º angle of soil shear resistance (Ha, 2007), the Rankine zone extends about 0.6 m from the fault plane.

Figures 12c, d, and e compare FE results with measured crown, invert, and bending strains, respectively, at 0.48 m of normal fault displacement for 1) 2D FE model (denoted as "2D Beam" in the figure), 2) 3D FE model with pipe shell elements and nonlinear springs for soil-pipe interaction (denoted as "3D Shell"), and 3) 3D FE model with pipe shell and continuum soil elements (denoted as "3D Cont."). The FE results for the 3D model are presented in the same format used by Xie et al. (2013).

All FE results show distributions similar to the measured ones. Both the 3D Shell and 3D Cont. models underpredict the maximum crown strain by 40% and 28%, respectively. In comparison, the 2D FE model underpredicts the maximum crown strain by 7%. Overall the 2D FE model results are comparable to the 3D model results, with maximum strains that are more consistent with measured maximum strains than those of the 3D models.

This finding differs from the conclusions presented by Xie et al. (2013) who found that 2D FE model predictions did not agree well with the measured strains. The 2D FE models applied in this work incorporate improvements with respect to the ASCE (1984) recommended soil-pipe interaction modeling procedures that were followed by Xie et al. (2013). The 2D FE model results in Figures 12c, d, and e incorporate the findings presented in this paper, which differ from the 2D FE modeling procedures followed by Xie at al. (2013) in four ways. First, coupled normal and frictional forces were modeled in the 2D FE analysis, using the FE setup in Figure 9 in contrast to the at-rest (K_0) conditions for longitudinal friction applied by Xie et al. (2013). Second, the 2D FE modeling used vertical downward forces from Figure 7 which are about 1/3

the magnitude derived from the conventional bear capacity approach presented in ASCE (1984). Reduction in the vertical downward soil reaction force is consistent with the findings of Xie et al. (2013) who recommend decreasing the vertical soil spring strength by a factor of 1/3 to 1/10 for 2D FE modeling of normal fault interaction with pipelines. Third, uplift forces decreasing after a peak force were modeled following the recommendations of Jung et al. (2013a). Fourth, a linear distribution of vertical displacement from the fault rupture to the end of the Rankine active zone on the upthrown side of the fault was used instead of abrupt vertical movement. This displacement pattern agrees with observations of surficial ground movement after the centrifuge test (Ha, 2007) and is consistent with active soil conditions that are mobilized near the upthrown side of a normal fault.

Conclusions

The principal causes of earthquake-induced ground deformation are identified and their interaction with underground infrastructure, primarily pipelines and conduits, is described. Methods for modeling soil-pipe interaction are reviewed with concentration on lateral, uplift, and vertical downward relative movement between pipe and soil. The fundamental mechanics of soil-pipe interaction are investigated through normal surface stresses measured with tactile pressure sensors during large-scale tests and the resolution of those stresses for normal and lateral force characterization. A procedure is developed for modeling coupled normal and longitudinal frictional forces on pipelines subject to permanent ground deformation, and a finite element configuration for coupled normal and frictional force modeling is presented. The effects of changing orientation between pipe and soil displacement at fault crossings and the margins of later spreads/landslides is investigated and quantified. Specific findings of interest are:

- The maximum downward pipe force is only about one-third the maximum force determined with conventional bearing capacity equations. The forces currently recommended in design are therefore overly conservative.
- Coupling normal and frictional forces in the numerical modeling of soil-pipe interaction is important for assessing the maximum axial pipe strain. Neglecting this coupled interaction through the sole use of at-rest (K_0) conditions for evaluating frictional force leads to underconservative results for axial strain.
- A simplified approach for modeling longitudinal friction along the pipe as the product of $\tan\delta$ and the soil reaction force normal to the pipe longitudinal axis is shown to provide an estimate that is either accurate or slightly conservative for analysis and design.

The analytical results for pipeline response to strike-slip fault rupture using the models developed in this work compare favorably with the results of large-scale tests of strike-slip fault movement imposed on 250-mm and 400-mm-diameter HDPE pipelines as well as centrifuge testing of normal fault movement on a 400-mm HDPE pipeline.

Acknowledgements

The work on which this paper was based was supported by the National Science Foundation (NSF) under Grant No. CMMI-1041498. Any opinions, findings and conclusions or recommendations expressed in this material are those of the authors and do not necessarily reflect the views of the NSF.

References

ABAQUS. *Theory Manual of ABAQUS*. ABAQUS Inc.: Providence, RI, 2014.

Akbas SO, Kulhawy FH. Axial compression of footings in cohesionless soils. I: Load-settlement behavior. *Journal of geotechnical and geoenvironmental engineering* 2009a; **135**(11): 1562-1574.

Akbas SO, Kulhawy FH. Axial compression of footings in cohesionless soils. II: Bearing Capacity. *Journal of geotechnical and geoenvironmental engineering* 2009b; **135**(11): 1575-1582.

ASCE. Guidelines for the seismic design of oil and gas pipeline systems. *Committee on Gas and Liquid Fuel Lifelines*, American Society of Civil Engineers: Reston, VA, 1984.

Bird J, O'Rourke TD, Bracegirdle A, Bommer J, Tromans I. A Framework for Assessing Earthquake Hazards for Major Pipelines 2004, *Proceedings, Intl. Conf. on Terrain and Geohazards Facing Onshore Oil and Gas Pipelines*, London, UK.

Chapra SC, Canale RP. *Numerical Methods for Engineers*. McGraw Hill: New York, 2006.

Ha D, Abdoun T, O'Rourke MJ, Symans MD ,O'Rourke TD, Palmer MC, Stewart HE. Buried high-density polyethylene pipelines subjected to normal and strike-slip faulting – a centrifuge investigation. *Canadian Geotechnical Journal* 2008; **45**(12)**:**1733-1742.

Ha D. *Evaluation of Ground Rupture Effects on Buried HDPE Pipelines*. PhD Thesis, RPI: Troy, NY, 2007.

Honegger D and Nyman DJ. *Guidelines for the Seismic Design and Assessment of Natural Gas and Liquid Hydrocarbon Pipelines*. Pipeline Research Council International; Catalog No. L51927, 2004.

Jung JK. Soil-pipe interaction under plane strain conditions. PhD Thesis, Cornell University: Ithaca, NY, 2010.

Jung JK, O'Rourke TD, Olson NA. Uplift soil–pipe interaction in granular soil. *Canadian Geotechnical Journal* 2013a; **50**(7): 744-753.

Jung JK, O'Rourke TD, Olson NA. Lateral soil-pipe interaction in dry and partially saturated sand. *Journal of Geotechnical and Geoenvironmental Engineering* 2013b; **139**(12): 2028-2036.

Kulhawy FH, Trautmann CH, Beech JF, O'Rourke TD, McGuire W, Wood WA, and Capano C. *Transmission Line Structure Foundations for Uplift/Compression Loading*. Electric Power Research Institute; Report EL-2870 1983: Palo Alto, CA.

Olson N. *Soil Performance for large scale soil-pipeline tests*. PhD Thesis, Cornell University: Ithaca, NY, 2009.

O'Rourke TD, Jezerski JM, Olson NA, Bonneau AL, Palmer MC, Stewart HE, O'Rourke MJ, Abdoun T. Geotechnics of pipeline system response to earthquakes. *Geotechnical Earthquake Engineering and Soil Dynamics IV (GEESD)* 2008: Sacramento, CA.

O'Rourke TD. Geohazards and large, geographically distributed systems. *Geotechnique* 2010; **60** (7): 505-543.

Palmer MC, O'Rourke TD, Olson NA, Abdoun T, Ha D, O'Rourke MJ. Tactile Pressure Sensors for Soil – Structure Interaction Assessment. *Journal of Geotechnical and Geoenvir. Engineering* 2009; **135**(11): 1638 – 1645.

Trautmann CH and O'Rourke TD. (1985). Lateral force-displacement response of buried pipe. *Journal of Geotechnical Engineering* 1985; **111**(9): 1068-1084.

Trautmann CH, O'Rourke TD, Kulhawy FH. Uplift force-displacement response of buried pipe. *Journal of Geotechnical Engineering* 1985; **111**(9): 1061-1076.

Xie X, Symans MD, O'Rourke MJ, Abdoun TH, O'Rourke TD, Palmer MC, Stewart HE. Numerical Modeling of Buried HDPE Pipelines Subjected to Normal Faulting: A Case Study. *Earthquake Spectra* 2013; **29** (2): 609-632.

Zienkiewicz OC, Emson C, Bettess P. A novel boundary infinite element. *International Journal for Numerical Methods in Engineering* 1983; **19**(3): 393-404.

Appendix A: Regression of Normalized Pipe Surface Stress Measurements

Curve fitting techniques described by Chapra and Canale (2006) for a sinusoidal function with angular frequency, ω_0, were used to derive an analytical expression for the normal stresses distribution. The least squares model follows the expression

$$y = A_o + A_1 \cos(\omega_o \theta) + B_1 \sin(\omega_o \theta) \tag{A.1}$$

in which $A_0 = \frac{1}{N}\sum_{i=1}^{N} y_i$, $A_1 = \frac{2}{N}\sum_{i=1}^{N} y_i \cos(\omega_o \theta_i)$, $A_2 = \frac{2}{N}\sum_{i=1}^{N} y_i \sin(\omega_o \theta_i)$, θ is the angular distance from the pipe crown, and N is the number of data points. The alternative form for Eq (A.1) is

$$y = A_o + C_1 \sin(\omega_o \theta + \Delta) \tag{A.2}$$

in which $\Delta = \varphi + \pi/2$, $\varphi = \tan^{-1}(-B_1/A_1)$, and $C_1 = (A_1^2 + B_1^2)^{1/2}$, which can be rearranged as

$$\sin^{-1}\left[\frac{y - A_o}{C_1}\right] = \omega_o \theta + \Delta \tag{A.3}$$

Letting $y = \left[p(\theta)/p_{\max}\right]$, the transformed normalized pressure, $\sin^{-1}\left[\frac{(p(\theta)/p_{\max}) - A_o}{C_1}\right]$ can be expressed as a linear function of θ in accordance with Eq. (A.3), in which ω_o and Δ are the slope and intercept, respectively, of the linear regression.